Metal Oxide-Based Photocatalysts for CO_2 Reduction

Subjects: Chemistry, Analytical

Contributor: Xuanzhen Li , Jing Xiong , Zhiling Tang , Wenjie He , Yingli Wang , Xiong Wang , Zhen Zhao , Yuechang Wei

The photoconversion of CO_2 into solar fuels seems to curb greenhouse effect and resolve the energy crisis. One of the challenges in developing practical CO_2 photoconversion catalysts is to design materials with a low cost, high activity and good stability. The excellent photocatalysts based on TiO_2, WO_3, ZnO, Cu_2O and CeO_2 metal oxides that are cost-effective and long-lasting were discussed. Strategies to improve CO_2 photoconversion efficiency are summarized and photocatalysts forms of 0D, 1D, 2D and 3DOM (zero/one/two-dimensional and three-dimensional-ordered macroporous, respectively) are involved, which can inspire the future improvement in photochemistry.

photochemistry CO2 reduction metal oxide materials solar fuels

1. Introduction

The transformation of CO_2 can be driven by illumination, electricity and heat [1]. Solar energy is a safe, clean, renewable and inexhaustible energy source, so it is ingenious to achieve this conversion with sunlight [2]. Additionally, the reaction conditions in photocatalytic processes are mild [3]; thus, it is easy to conduct experimental tests. A new world opened up since H_2 and O_2 were obtained after radiating TiO_2 with light. Extensive research about photocatalyst were conducted until the year of 2000. Since then, a growing number of materials have been designed and studied to absorb solar energy, including oxide semiconductors, sulfides (ZnS, CdS and MoS_2), and polyoxometalates (Bi_2WO_6, Bi_2MoO_6 and $BiFeO_3$) [4][5]. Organics, organometallic complexes, covalent organic polymers and noncovalent self-assembled supramolecular organic matter are also involved. Among them, inorganic metal oxide materials are widely studied for establishing efficient artificial photosystems due to their low cost, facile synthesis, stable crystal structures and environmental friendliness. TiO_2, Cu_2O, ZnO, WO_3 and CeO_2 show promising research value as the most common materials.

2. Theoretical Foundation and Strategies of Photocatalytic CO_2 Reduction

The photocatalytic process in semiconductors can generally be described as shown in **Figure 1**. Upon being excited by an incident photon with energy equal to or higher than the bandgap (*E*g), charge carriers are generated. Electrons (e^-) at the bottom of conduction band (CB) migrate to the surface of the catalyst to initiate reduction reactions with CO_2. Holes (h^+) at the top of valence band (VB) conduct oxidative reactions.

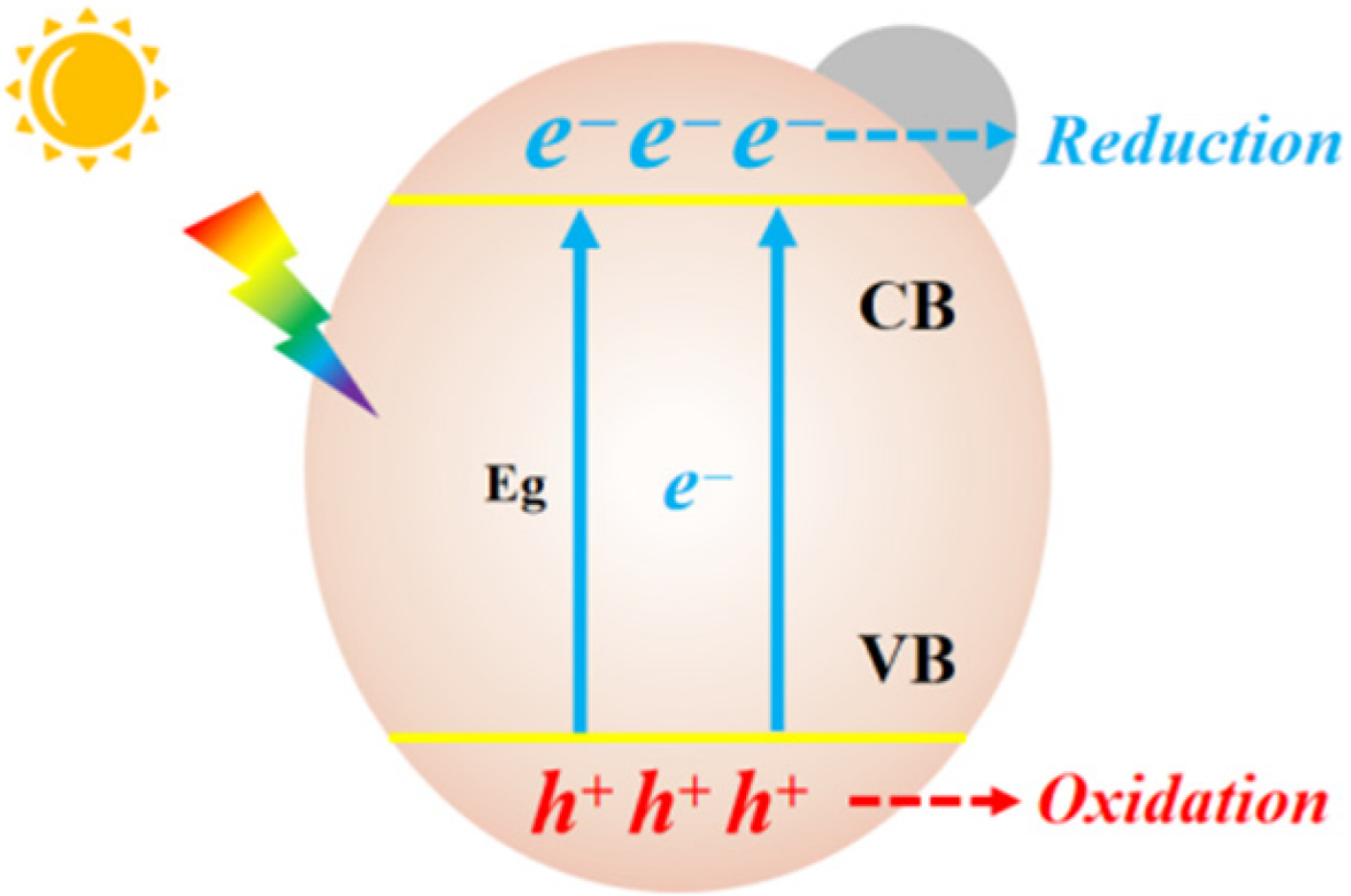

Figure 1. Fundamentals of photocatalytic reduction on a semiconductor catalyst.

The photocatalytic process of CO_2 conversion on semiconductors can be divided into five general steps: (1) Formation of electron–hole pairs under light radiation, (2) Separation and migration of the electrons and positive holes, (3) Adsorption and activation of CO_2, (4) Redox reactions between surface-adsorbed species and electron–hole pairs, and (5) Desorption of the product. The electrochemical reactions with standard oxidation–reduction potentials (at pH 7 vs. NHE) are as follows:

$$H_2O + h^+ \rightarrow OH\bullet + H^+ \quad (1)$$

$$H^+ + e^- \rightarrow H\bullet \quad (2)$$

$$H\bullet + H\bullet \rightarrow H_2 \quad (3)$$

$$CO_2 + e^- \rightarrow CO_2^- \quad (4)$$

$$CO_2 + 2H^+ + 2e^- \rightarrow HCOOH,\ E_0 = -0.61\ V \quad (5)$$

$$CO_2 + 2H^+ + 2e^- \rightarrow CO + H_2O,\ E_0 = -0.53\ V \quad (6)$$

$$CO_2 + 4H^+ + 4e^- \rightarrow HCHO + H_2O,\ E_0 = -0.48\ V \quad (7)$$

$$CO_2 + 6H^+ + 6e^- \rightarrow CH_3OH + H_2O,\ E_0 = -0.38\ V \quad (8)$$

$$CO_2 + 8H^+ + 8e^- \rightarrow CH_4 + 2H_2O,\ E_0 = -0.24\ V \quad (9)$$

To carry out the conversion, it is necessary to comprehend the structure of CO_2. Due to the great symmetry and high bond energy of 750 kJ/mol, it is particularly difficult to break the C=O double bond. Therefore, the transmutation between CO_2 and bent radical anion of $CO_2^{\bullet-}$ on the surface of the catalyst is widely recognized as the first step to activate CO_2 for subsequent reaction. Additionally, photoreactions occur favorably only when the CB position of the catalyst presents a more negative potential than the target reduction and the VB position is more positive than the oxidation reaction. **Figure 2** summarizes the current strategies that can boost the photocatalytic CO_2 reduction pace, with detailed information being presented sequentially below.

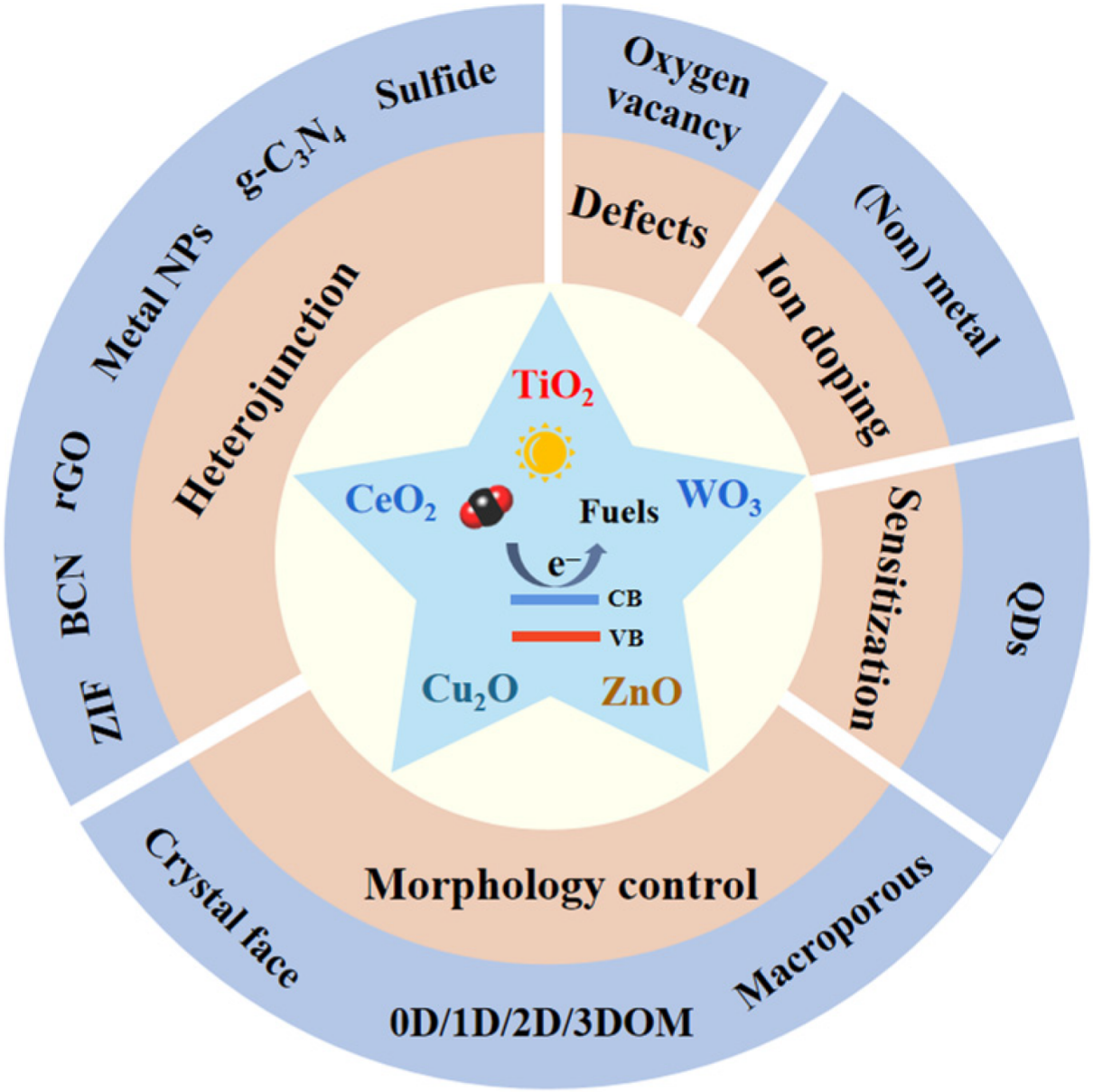

Figure 2. Strategies to boost the photocatalytic CO_2 reduction.

2.1. Morphological Control

The surface topography of nanocrystals could evidently alter the electronic structure, surface energy and chemical properties of catalysts. Therefore, morphological control is one of the most important issues to researchers in nanoscience, chemistry and physics. Open facets and edges determine the shape of nanocrystals. Thus, the preferential adsorption of additives on certain crystal surfaces provides a good opportunity to tune the surface of nanomaterials.

2.1.1. Exposed Facet Adjustment

Exploring and figuring out the variation that is connected with exposed surfaces is crucial to elucidate shape-related chemical and physical properties. In semiconductor crystals, different facets have distinct electronic band structures that influence the transport of photoexcited carrier charges. It is wise to expose active facets to tune the CO_2 photoreduction efficiency [6].

2.1.2. Quantum Dots (QDs)

Zero-dimensional (0D) semiconductor quantum dots (QDs) have many unique properties, such as quantum confinement effect, high extinction coefficient and multiple exciton generation [7]. Hence, QDs show much better photoactivity in the visible light region. Unlike bulk materials, surface atoms make up the majority of QD semiconductors. The abundant surface sites enhance the interaction between electron donors and acceptors, thus facilitating the photocatalytic charge transfer.

2.1.3. One-Dimensional and Two-Dimensional Structures

One-dimensional nanostructured catalysts have high aspect ratios, such as nanowires, nanorods and nanotubes. The morphological tuning of the material makes a difference to their thermal, optical, electrical and magnetic properties [8]. For instance, TiO_2 nanotube can act as a channel for electron transfer and build up the chemical reactions rate.

Two-dimensional layered materials can protect a tiny particle component from aggregation. The CO_2 adsorption capacity on 2D photocatalysts can be enhanced due to the large specific surface area and bountiful surface defects [9]. Two-dimensional lamellar nanosheets are widely used in photocatalysts, such as g-C_3N_4, MoS_2 and WO_3.

2.1.4. Macroporous and Three-Dimensional Ordered Macroporous (3DOM) Structures

Macroporous materials are widely used in photocatalytic materials, owing to their excellent properties [10]. Unlike dispersed particles, sunlight can penetrate the pore wall easily and scatter widely inside the hollow structure, thus increasing the efficiency of illumination. Subsequently, the slender walls of pore reduce the transfer length of photo-

generated charge carriers. Electrons (e^-) and holes (h^+) are separated more efficiently when heterojunctions are loaded on porous materials. The specific surface it provides is so large that more CO_2 molecules have a chance to contact the catalyst for reduction reactions.

Growing attention has been paid to hierarchical composite pores, including photonic crystal catalysis and separation of sub-microns. The slow light effect of photons associated with 3DOM materials have been considered to increase solar radiation absorption and enhance photocatalyst performance [11]. 3DOM products with periodic macrostructures [12], known as inverse opal, have been applied in battery materials, sensors, separation engineering and heterogeneous catalysis.

2.1.5. Preparation of 3DOM Materials

Specifically, 3DOM materials are produced by the colloidal crystal template (CCT) method (**Figure 3**). Firstly, a uniform and close-connected organic sphere template can be obtained, through three key processes. Then, seeping metallic salt sol into the void of microspheres. After heat treatment, the organic microsphere template fades away and leaves a metal oxide frame. (i) The polymerizable monomer (methyl methacrylate, styrene) and initiator are mixed and heated under the protection of Ar; (ii) the earlier reaction liquid is filtered with microfiltration membrane; (iii) the microsphere mixture is centrifuged at a high speed for a long time, yielding the polymethylmethacrylate (PMMA) or polystyrene (PS) template; (iv) the template is immersed in the precursor solution and (v) is calcinated.

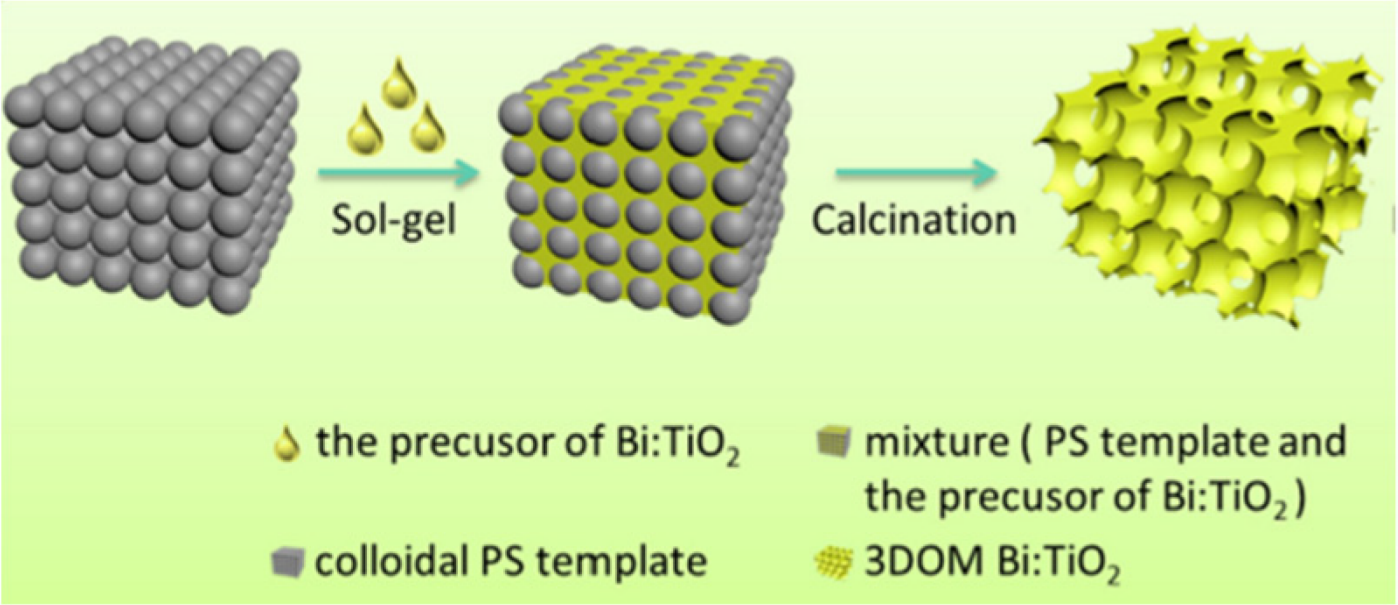

Figure 3. The fabrication process of the 3DOM Bi-doped TiO_2 [13].

2.2. Heterojunction

Photogenerated charge carriers in a single material tend to recombine rapidly due to Coulombic force and they can be separated efficiently in the multi-materials that are in close contact [14]. The heterojunction is an interface

between various semiconductors with different energy band structures. The heterojunction structure can reduce the probability of charge recombination and is therefore considered an effective method to enhance the photocatalytic activity [15][16].

2.3. Defects

All semiconductors have surface defects, which are rooted in the absence of host atoms. The amount of oxygen vacancies can be altered by ion doping and nanocrystal modifications. Oxygen defects and other defects [17] can facilitate the separation of h^+/e^-. Over and above, defects can also activate CO_2 molecules, reducing the activation energy of the reaction [18].

2.4. Ion Doping

Elemental doping is a common strategy to modulate the surface electronic structure. Then, the band gap of the semiconductors make a difference, nonmetal doping (such as N, C and O) mainly alters the VB and metal-doping (e.g., Mo, Co and Ni) influences the CB [19][20]. For example, Cu-doped TiO_2 absorbs more visible light due to the Cu 3d-Ti 3d optical transition [21].

2.5. Sensitization

Sensitization means coupling the quantum dots, dyes, etc., with semiconductors to increase the photogenerated carriers and promote the absorption of light by taking advantage of their receptivity in UV, visible or infrared light.

3. Photocatalysts with Different Basis Matrices

3.1. TiO_2-Based Photocatalysts

Titanium dioxide (TiO_2) is notable in photochemistry, with advantages such as non-toxic, cheapness, corrosion resistant, good physical and chemical stability. However, owing to the wide E_g of 3.0–3.2 eV, TiO_2 only absorbs energy in the ultraviolet region (3–5% of the solar energy), and photoexcited charge pairs are easy to combine, resulting in quantum inefficiency. Usually, TiO_2 is divided into the rutile, anatase and brookite on the basis of atomic arrangement modes. Rutile TiO_2 is thermodynamically stable and does not distort or decompose at high temperatures. It has a narrower energy gap (3.0 eV) and a wider spectral response than the anatase phase (3.2 eV). Rutile TiO_2 seeds generally grow larger in size and tend to form an agglomerated structure. Smaller anatase TiO_2 particles have a wider lattice gap and abundant surface oxygen defects, which make it favorable for ion doping and photoreactions.

3.1.1. Morphological Control

In hollow nanotube-shaped catalysts, the transport speed of CO_2 and photoproducts can be facilitated. Ru phase is inclined to form methane in CO_2 hydrogenation process [22] and Yang et al. [23] entrapped Ru nanoparticles in TiO_2

nanotubes. Restricted Ru nanoparticles were resistant to sintering and leaching in the Ru-in/TNT catalyst channel (**Figure 4**). Electrons tend to gather in the tubes because of a confinement effect, which leads to an abundant, accessible metallic phase. It is easier for high-priced Ru species to combine with free electrons and then exhibit a superb CH_4 and CH_3OH yield.

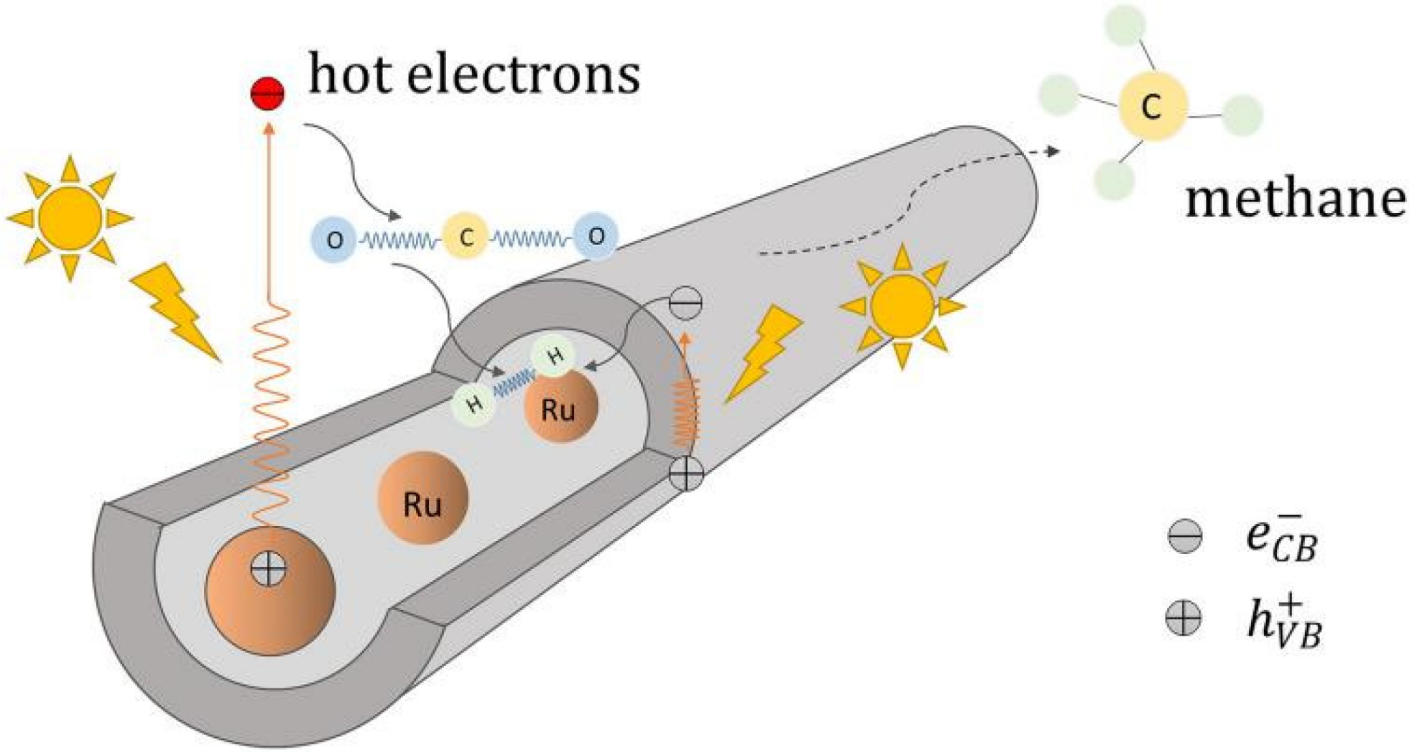

Figure 4. The reaction pathway for the Ru entrapped in the TiO_2 nanotubes catalyzes CO_2 methanation [23].

On the contrary, Kar et al. [24] loaded metal nanoparticles onto vertically oriented 1D TiO_2 nanotube arrays (TNAs) platforms via the graft method. In the synthesis process, Au, Ru and ZnPd NPs grow anodically on transparent glass substrates. There is no band bending phenomenon in Au NP-grafted TiO_2, which can be observed from ultraviolet photoelectron spectroscopy (UPS). TPD experiments proved that all NP-grafted samples absorb more CO_2 than TNAs. It is worth noting that, in nanoparticle-grafted TNAs, blue photons close to and below the TiO_2 band edge were excited to drive CO_2 photoreduction process. Ru-TNAs, ZnPd-TNAs and Au-TNAs had the CH_4 formation rates of 26, 27 and 58 $\mu mol \cdot g^{-1} \cdot h^{-1}$, respectively.

Metal–organic frameworks (MOFs), also known as porous coordination polymers, composed of organic linkers and metal nodes (metal ions or clusters), are a kind of porous crystalline inorganic–organic hybrid materials. The unique advantages of MOFs, such as extremely high surface area, uniform adjustable porous structure and high density coordination unsaturated metal sites, have been extensively researched.

Exposed Facet Adjustment

A Pt-TiO_2 single atomic site catalyst (PtSA/Def-s-TiO_2) was prepared [25] by the “thermal solvent-argon treatment and hydrogen reduction” method. In order to construct Ti–Pt–Ti structures, TiO_2 nanosheets with oxygen deficient sites were used to anchor monatomic Pt particles, which can retain the stability of isolated single atomic Pt and improve photocatalytic performance. The exposed (101) and (001) crystalline of TiO_2 nanosheets were determined by transmission electron microscopy, and a thickness of 6.9 nm was observed through atomic force microscope. The EPR spectra of the samples confirm that the rich oxygen defect structure can be obtained by heating TiO_2 nanosheets in argon atmosphere.

3DOM Structure Ti-Based Materials

A ternary 3DOM Bi-doped TiO_2 photocatalyst decorated with carbon dots (CDs) was obtained, whose pore engineering of the 3DOM skeleton greatly promoted the response in the whole solar spectrum range [13]. It exhibits enhanced photocatalytic performance because of its excellent exquisite structure and high charge transfer efficiency. Similarly, a $BiVO_4$/3DOM TiO_2 nanocomposite [26] was synthesized as a highly efficient photocatalytic catalyst for the degradation of dye pollutants.

3.1.2. Heterojunction

p–n heterojunction: A p–n heterojunction is formed by combining p-type and n-type semiconductors. Even without light irradiation, electrons can diffuse from an n-type semiconductor to a nearby p-type one, in the case of the combination of two materials. Correspondingly, the holes on the surface of a p-type semiconductor are transferred to the n-type one, which results in an efficient separation of charge carriers. A $ZnFe_2O_4$-modified TiO_2 was synthesized by the hydrothermal method [27], and the p-n heterojunction system could reduce CO_2 to methanol at a yield of 75.34 μmol g^{-1} h^{-1}.

rGO composite: graphene materials have been widely used because of their large specific surface area, unique thermal stability and excellent electrical conductivity. Graphite nanomaterials are visible-light-responsive materials with appropriate band gaps, and the energy levels of CB and VB are in optimal positions relative to ordinary hydrogen electrodes. These unique photocatalytic properties have made them prime candidates for photocatalytic CO_2 reduction. Fortunately, tightly contacted ultra-thin graphene layers and TiO_2 compounds and can be prepared with some additives [28].

3.1.3. Ion Doping

In recent years, elements such as B, N, Co and Bi have been widely applied in TiO_2 doping. A carbon-based hybrid nanocomposite reduced graphene oxide (rGO), belonging to the narrow band gap, with oxygen-containing functional groups on the surface that can be enhanced by π interactions [29]. Laminar graphene carriers not only prevent TiO_2 repolymerization, but also hybridize the function of the catalytic system. Co-doped TiO_2 was loaded on the rGO [30], and the Co peak in EDX spectra and C-O peak in FT-IR spectra confirmed the successful doping and the presence of graphene support, respectively. The size of TiO_2 particles decreased from 48–80 nm to 23–28 nm, which is consistent with earlier reports of changes in titanium doping with transition metal ions.

3.1.4. Sensitization

A growing number of semiconductor materials are used to modify TiO_2, but randomly mixed catalysts are not stable enough to achieve reproducibility. Therefore, Lee [31] grew well dispersed p-type NiS nanoparticles on the surface of a highly aligned n-type TiO_2 film to obtain the NiS-sensitized TiO_2 films. The band gaps of two components were estimated by wavelength relation. Some inferences can be drawn when considering the results of both the ultraviolet and visible spectra. It indicates that more electrons are subpoenaed from the short-E_g NiS and transferred to TiO_2 conduction band. The spectra results reconfirmed the electron contribution of the NiS and the design of a catalyst that produced 3.77-fold CH_4 compared to the TiO_2 film.

3.2. WO_3-Based Photocatalysts

Tungsten-based oxides (WO_3) have been extensively studied in recent decades and various morphologies have been presented. In the WO_3 structure, the crystal in the stoichiometric ratio is connected with a twisted WO_6 octahedra to form a perovskite crystal structure. It has monoclinic, orthorhombic and hexagonal crystal forms. At the same time, the oxygen lattice can be lost easily, resulting in oxygen vacancies and coordinatively unsaturated W atoms. Therefore, tungsten oxide has many non-stoichiometric compounds, such as $WO_{2.72}$, $WO_{2.8}$, $WO_{2.83}$ and $WO_{2.9}$.

3.2.1 Morphological Control

Bi_2WO_6 is one of the tungsten-based materials that belongs to Aurivillius crystal oxides. Its crystal has an orthorhombic system, and its narrow band gap (2.7–2.9 eV) structure allows it to meet the response absorption of visible light. Moreover, its stable structure and eco-friendly properties have attracted many scientific researchers to study it. Since the valence band of Bi_2WO_6 is composed of O_{2p} and Bi_{6p}, and the conduction band is composed of W_{5d}-assisted Bi6p orbitals, the VB energy levels can be dispersed broadly. By employing the Kirkendall effect in ion exchange and BiOBr precursor, Huang et al. [32] prepared a bowl-shaped Bi_2WO_6 HMS material. Based on the large specific surface area of the material, its adsorption capacity for CO_2 reaches 12.7 mg g^{-1} at room temperature and pressure. The material adsorbs a large number of HCO_3^- and CO_3^{2-} species on the surface during the reaction, which makes the catalytic reaction easier. The Bi_2WO_6 HMS thus has a high catalytic activity, and the methanol yield is 25 times higher than that of the Bi_2WO_6 SSR.

Iron phthalocyanine FePc is neatly assembled on porous WO_3 under induction and coupled with surface atoms by H-bonding [33]. The optimized FePc/porous WO_3 nanocomposites exhibit enhanced CO_2 photoreduction activity, which is attributed to the synergistic effects of a high specific surface area, a better charge separation and proper central metal cation. A series of mesoporous WO_3 with interconnected networks were synthesized by the silica KIT-6 hard template method [34], which became oxygen-deficient after hydrogenation treatment. Both the ordered porous structure and oxygen vacancies contributed to the increased yield of CH_4 and CH_3OH.

WO_3 with a hollow nest morphology with hierarchical micro/nanostructures (HNWMs) was synthesized [35] by the one-step hydrothermal method (**Figure 5**), with a particle diameter of about 2.5 μm. The 2D nanosheets, which

have an average thickness of 30–40 nm, were assembled to build a distinctive hollow nest structure with a good stability and reusability under visible light. Hao et al. [36] prepared core–shell heterojunctions of two-dimensional lamellar $WO_3/CuWO_4$ by the in situ method. After the modification of amorphous Co-Pi co-catalyst, the photoanode of ternary homogeneous core–shell structure exhibited a high photocurrent of 1.4 mA/cm^2 at 1.23 V/RHE, which was 6.67 and 1.75 times higher than that of the pristine WO_3 and 2D homogeneous heterojunction.

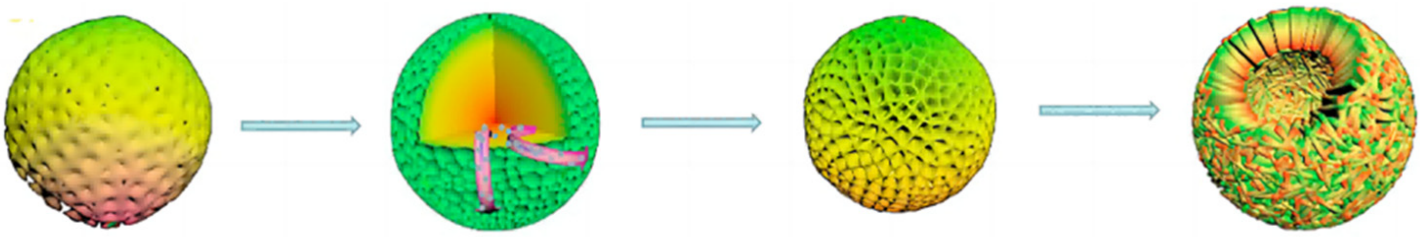

Figure 5. Schematic diagram of the HNWM formation process [35].

Ti atoms in ultrathin Ti-doped WO_3 nanosheets promoted the charge transfer [37], as they accelerate the generation of key intermediates COOH*, which was revealed by in situ characterization. Furthermore, Gibbs free energy calculations were calculated to verify that ion doping can reduce the CO_2 activation energy barrier and CH_3OH desorption energy barrier by 0.22 eV and 0.42 eV, respectively, thus promoting the formation of CH_3OH. The ultrathin Ti-WO_3 nanosheets showed an excellent CH_3OH yield of 16.8 μmol g $^{-1}$ h $^{-1}$. Two-dimensional bilayered WO_3@$CoWO_4$ were prepared [38] via a facile interface-induced synthesis method. The optical energy conversion efficiency can be improved by both p–n heterojunctions and interfacial oxygen vacancies. The narrow band gap of the WO_3@$CoWO_4$ heterojunction was proved by DFT calculations and some characterizations, which allows a better visible light absorption. A tree-like WO_3 film was prepared [39] by the hydrothermal process, which has a large specific surface area. The WO_3 product was a unity of hexagonal/monoclinic crystals, which contained W^{5+} defects and oxygen vacancies. The products were further subjected to a mild reduction solution at the lower temperature of 333 K to introduce more defects.

Preferentially Exposed Facets

According to studies, infrared (IR) light makes up nearly 50% of solar energy, and it is challenging to make use of the majority of the light. Liang et al. [40] fabricated 2D ultrathin WO_3 with an intermediate band gap. They achieved the first complete decomposition of CO_2 driven by infrared light without the addition of sacrificial agents. Theoretical calculations indicated that the generation of the intermediate energy band resulted from the critical density of the generated oxygen vacancies, which has also been verified by synchrotron valence band spectroscopy, photoluminescence spectroscopy, ultraviolet-visible-near-infrared spectroscopy and synchrotron infrared reflection spectroscopy.

3DOM Structure W-Based Materials

Unexpectedly, it was found that the resistance of 3DOM-WO_3(270) and the Ag_3PO_4 electron absorption band were comparable. By depositing Ag_3PO_4 nanoparticles in the micropores of 3DOM-WO_3, Chang et al. [41] achieved a

higher photocatalytic activity and more efficient light harvesting at the wavelengths of 460–550 nm. A Z-scheme g-C_3N_4/3DOM-WO_3 catalyst designed by Tang et al. [42] also has a high CO_2 photoreduction activity.

3.2.2. Heterojunction

Quantum dot composite: CuO quantum dots (QDs) were combined with WO_3 nanosheets by a self-assembly method and the diameter of 6%CuO QDs/WO_3 NSs was mainly located at 1.6 nm [43]. The bandgap energy of CuO/WO_3 fell in 2.28 eV and the complex catalyst possessed a lower resistance for charge carrier transfer that showed in UV-vis DRS and EIS analysis. Due to the low CB position, CO cannot be obtained when using pure WO_3. However, the photogenerated electrons gathered in the WO_3 CB position was able to reach the CuO VB position when the Z-scheme (**Figure 6**) was formed by intimate heterojunctions. At the same time, the reduction reaction that transformed CO_2 into CO occurred at the CuO CB position.

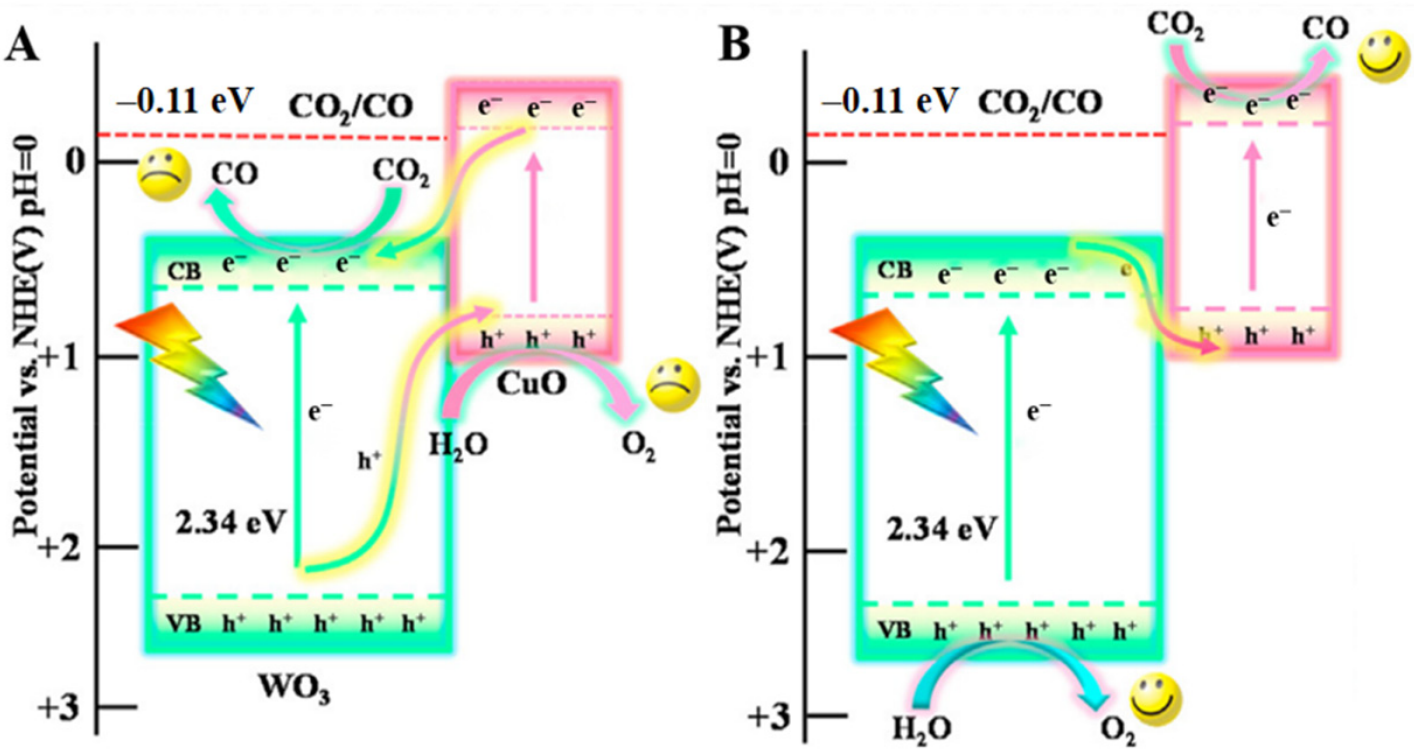

Figure 6. The proposed charge transfer mechanisms: (**A**) Ⅱ-scheme and (**B**) Z-scheme for CuO/WO_3 [43].

3.2.3. Ion Doping

Molybdenum with a similar ionic size was chosen to dope the WO_3 as a low-valence metal species. The W^{5+}/W^{6+} ratio of the catalyst was increased, making it easier to exchange electrons with reactants. The conductivity of protons was enhanced by the presence of hydrogen bronze, which originated from a chemical reaction between WO_3 and Brønsted protons and excess electrons in their lattices.

3.3. ZnO-Based Photocatalysts

ZnO, a common metal oxide, is a n-type semiconductor with an E_g value of 3.37 eV. It is a kind of amphoteric oxide that has the advantages of nontoxic harmlessness, low cost, abundant reserves, convenient preparation, low dielectric constant and low optical coupling rate. ZnO has three main lattice structures: wurtzite structure, zinc-blended structure and tetragonal rock salt structure. The wurtzite structure is considered the most stable and common structure in nature. It is a kind of hexagonal crystal, in which the O and Zn atoms are aligned with the hexagonal density stacking.

3.3.1. Morphological Control

The 3nm Pt particles were uniformly dispersed over ZnS@ZnO with a mesoporous heterostructure [44] and more CH_3OH was obtained. Reactant charge carriers entered the pore channels of the porous heterozygous layer, thus reducing the likelihood of flow resistance and electron–hole recombination. The S-scheme photocatalyst delivered a high CH_3OH formation rate of 81.1 μmol g^{-1} h^{-1}, which is roughly 40 and 20 times larger than that of bare ZnO (3.72 μmol g^{-1} h^{-1}) and ZnO–ZnS (4.15 μmol g^{-1} h^{-1}). On the other hand, a porous ZnO@ZnSe core/shell nanosheet array material (**Figure 7**A) was prepared in a controlled manner [45]. The final n-type semiconductor composites had a proper negative CB band edge. In comparison to ZnO or ZnSe, more pairs of electron–holes were formed under visible light. Electrons tend to land on ZnO, which is aimed at methanol production. Mei et al. prepared a ZnO microsphere with different numbers of shells [46] and the photoelectric performance of ZnO was optimal when the number of shells reached three.

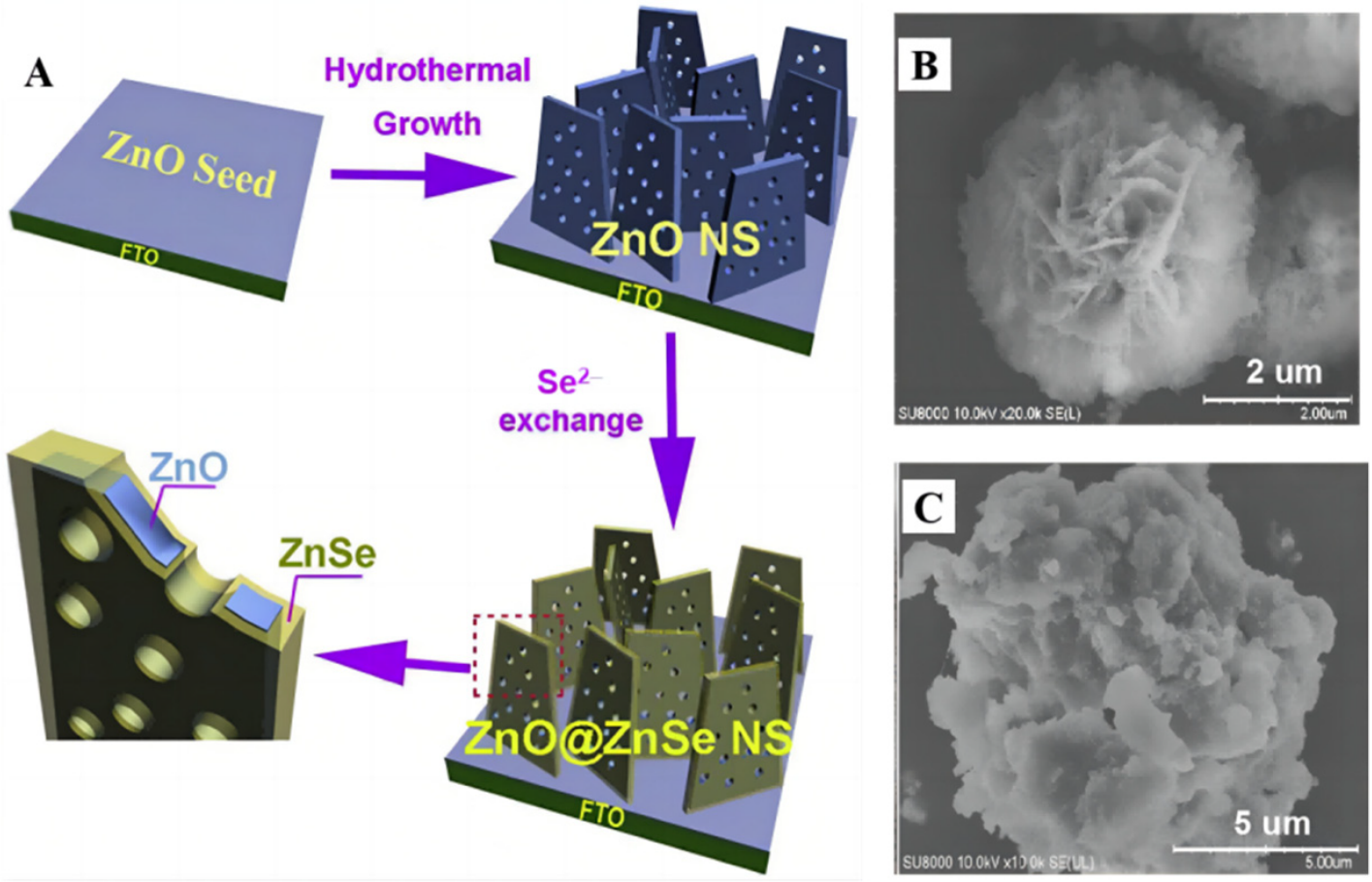

Figure 7. (**A**) Schematic illustration of the fabrication process of ZnO@ZnSe photocathode [47]. (**B**) ZnO/ZnS (**C**) ZnO/ZnS/g-C_3N_4 SEM images [45].

ZnO/ZnS nanoflowers (**Figure 7**B) were combined with g-C_3N_4 nanosheets (**Figure 7**C) to construct a double Z-scheme structure [48]. ZnO/ZnS nanoflowers provide a large specific surface area and g-C_3N_4 helps to absorb more photons under solar light irradiation. Optimized interfacial charge transfer dynamics in ternary heterostructure can be characterized by photocurrent measurements. As a result, the formation rate of H_2 product over the novel double Z-scheme mixture increases to 301 μmol g^{-1} h^{-1} on water splitting.

3DOM Structure Zn-Based Materials

Wang et al. [49] published metal-organic-framework-derived 3DOM N-C doped ZnO (**Figure 8**) for efficient CO_2 reduction. The ultra-tiny CoO_x clusters were anchored on the surface of catalyst and no Co-Co peak was found in CoO_x/N-C-ZnO. The charge transfer rate was jacked up by ion doping and the recombination of electron-hole pairs was tamed because of the CoO_x clusters. Furthermore, CoO_x on the orderly connected channels can act as an electron trap to capture electrons, which makes a contribution to photoreaction efficiency. The density theory calculations (DFT) was also used to detect the CO_2 adsorption ability, and CoO_x/N-C-ZnO exhibited the most negative CO_2 binding energy due to improved electron structure of adsorption site.

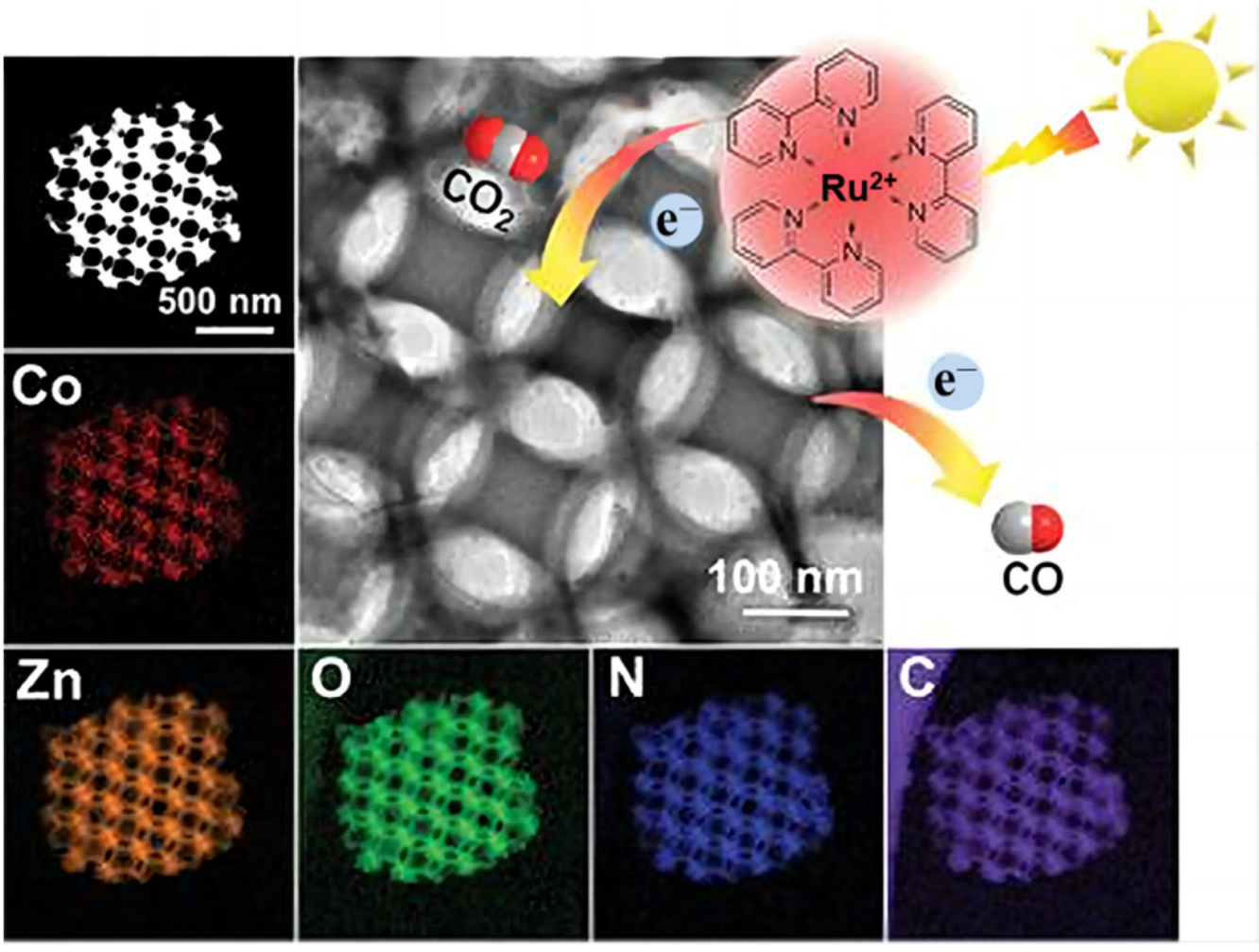

Figure 8. HAADF-STEM image of CoO_x/N-C-ZnO and related elemental mapping images [49].

3.3.2. Heterojunction

Recently, zeolitic framework (ZF) composite fabricated by the microwave-hydrothermal synthesis method (MWH) has attracted attention, which can provide a fast heating-speed and produce morphologically uniform samples. With biodegradable template, the zeolitic framework (ZF) was synthesized via MWH method from volcanic ashes. The $NaAlSiO_4$ (NAS) framework was composed of 50 nm circular channels and has a large surface area. The synergistic effect among ZnO, CuO and ZF support accelerated the photocatalytic process of CO2 reduction, which offers higher HCOOH evolution rate.

3.4. Cu_2O-Based Photocatalysts

Cuprous oxide (Cu_2O) is a potential p-type semiconductor with a wide visible-light response range and high photo-electric conversion efficiency (18%) [50], and it displays attractive prospects in solar energy conversion and heterogeneous photocatalysis. Although Cu_2O possesses many excellent properties, photocorrosion and the rapid recombination of e^-/h^+ pairs affect its activity and limit its application. The photocorrosion is believed to occur in two ways: (1) self-reduction caused by generated electrons and (2) self-oxidation caused by the generated holes.
Self-reducing photocorrosion:

$$Cu_2O + H_2O + 2e^- \rightarrow 2Cu + 2OH^- \quad (10)$$

Self-oxidative photocorrosion:

$$Cu_2O + 2OH^- + 2h^+ \rightarrow 2CuO + H_2O \quad (11)$$

Therefore, developing Cu-based catalysts with excellent activity, selectivity and stability has become the research hotspot in the area of the photocatalytic reduction of CO_2. Many successful attempts have been made to improve the photostability and photocatalytic performance of Cu_2O. In general, most studies focus on enhancing the charge transfer from Cu_2O to reactants or cocatalysts to prevent charges from accumulating within the particles.

3.4.1. Morphological Control

A branch-like $Cd_xZn_{1-x}Se$ nanostructure was obtained [51] by the cation-exchange method, which was then mixed with Cu_2O@Cu to form heterojunctions. Selenium (Se) vacancies were created during the ion exchange process and the crystal growth was limited due to the additive diethylenetriamine (DETA), leading to insufficient coordination of the surface atoms, which then become active adsorption sites. Highly hierarchical branching-like structures assembled by one-dimensional structural materials not only facilitate electron accumulation at their tips but also increase the light-accepting area, and characterization results show that branching structures can effectively absorb visible light. $Cd_{0.7}Zn_{0.3}Se/Cu_2O$@Cu step-scheme heterojunction exhibited a CO release yield of 50.5 μmol g^{-1} h^{-1}.

Ultrafine cuprous oxide U-Cu_2O (<3 nm) was grown on the polymeric carbon nitride (PCN) (**Figure 9**) by the in situ method [52]. PCN has a narrow band gap of 2.7 eV that can capture visible light. Both ultrafine nanoclusters and Z-scheme heterojunction can protect U-Cu_2O from degradation. The photocatalyst U-Cu_2O-LTH@PCN has high stability, maintaining more than 95% activity after five cycles of testing, while bare Cu_2O grades completely within three cycles. A large number of heterojunctions were formed by U-Cu_2O particles and lamellar PCN, expediting the electron transfer efficiency. The product can convert CO_2 to methanol with water vapor under light irradiation at the high yield of 73.46 μmol g^{-1} h^{-1}.

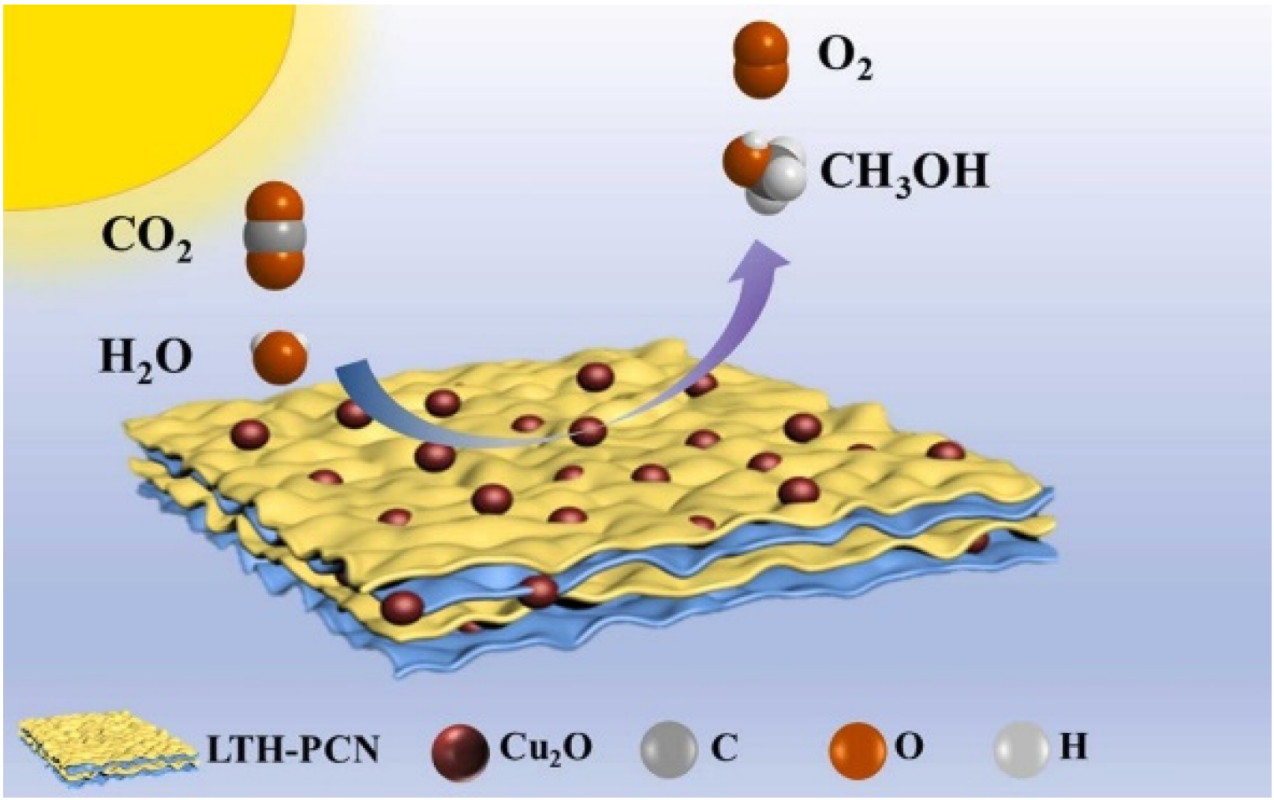

Figure 9. Ultrafine U-Cu_2O nanoclusters anchored on the photosensitizing PCN support [52].

Preferentially Exposed Facets

Cu_2O is an ideal compound to study the influence of electron-related effects. The rare occurrence of the O-Cu-O 180^o linear coordination of Cu_2O makes its (111), (100) and (110) facets chemically active. Zhang et al. [53] successfully achieved the morphology control of Cu_2O nanocrystals by utilizing the selective surface stabilization of PVP on the (111) plane of Cu_2O. With different amounts of PVP, the surface area ratio of (111) to (100) was subtly tuned, which resulted in the shape evolution of the system and various Cu_2O structures (**Figure 10**). The detailed modification mechanism was elucidated from the structural and kinetic perspectives.

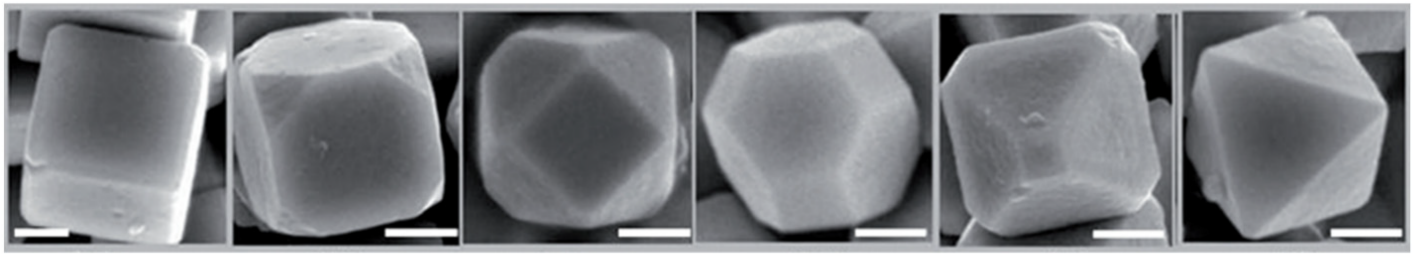

Figure 10. FESEM images of the Cu_2O polyhedrons with different volume ratios of (100) to (111) [53].

3DOM Structure Cu-Based Materials

The 3DOM Cu_2O structure was luckily obtained [54] via polystyrene crystal templates. Under the contrived "sunlight" irradiation, incident light was reflected and absorbed around and around again. In the ultra-visible absorption spectra (350 to 800 nm), Cu_2O with large orifices absorbs more photons than bulk samples, making it more advisable for solar applications. 3DOM Cu_2O was prepared [55] by the electrochemical method to reduce CO_2, and its Faraday efficiency was five times higher than that of Cu film. The $CO_2{\cdot}^-$ intermediate in 3DOM channels is more stable and leads to the possibility of forming CO and HCOOH products (**Figure 11**).

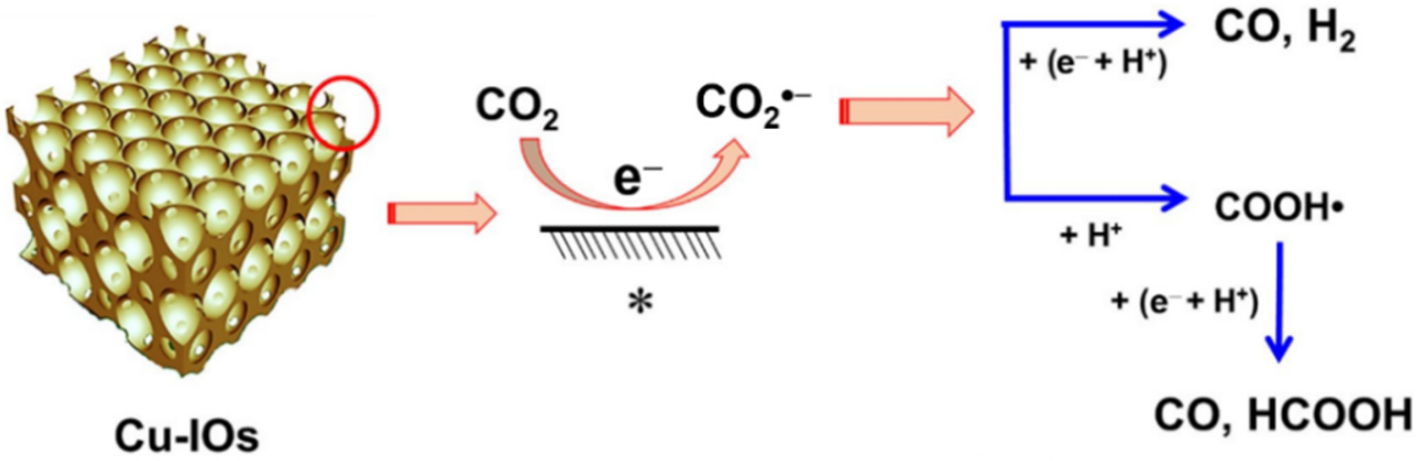

Figure 11. Proposed mechanism for CO_2 reduction to CO and HCOOH on Cu_2O-derived Cu-IOs (The symbol "*" represents the surface.) [55].

3.4.2. Heterojunction

Liu et al. [56] reported a facile solution and chemistry route to synthesize rGO-incorporated crystal Cu_2O with various facets as visible-light-active photocatalysts for CO_2 reduction. The enhanced activity was attributed to the formation of the heterojunction and the existence of rGO as the electron transport mediator. M. Flores et al. [57] adopted the microwave-hydrothermal method to couple the powders of $Mg(OH)_2$, CuO and Cu_2O. The synthesis method allowed a sufficient interaction between $Mg(OH)_2$/CuO and Cu_2O without inhibiting the gas adsorption capacity of $Mg(OH)_2$. They found that the presence of Cu_2O favored the selectivity towards CH_3OH production because a higher Cu^+ concentration led to better selectivity.

3.5. CeO_2-Based Photocatalysts

Cerium oxide (CeO_2) has an octahedral face-centered cubic fluorite structure, in which the coordination numbers of Ce and O are 8 and 4. When reduced at a high temperature, it can be converted to nonstoichiometric CeO_{2-x} ($0 < x < 0.5$). Notably, CeO_{2-x} maintains a fluorite crystal structure and forms oxygen vacancies after losing a certain amount of oxygen. CeO_{2-X} materials with different Ce/O ratios were also obtained in different conditions and it could be reconverted to CeO_2 again if it returned to an oxidizing environment. Because of the unique electrical structure, cerium oxide (CeO_2) is famous for the conversion sates between Ce^{4+} and Ce^{3+}, which have been studied as oxygen storage catalytic materials and solid oxide full cells by many scholars [58][59]. In summary, CeO_2 is a rare-earth metal oxide with a good photochemical stability, low cost and environment friendly characteristics.

3.5.1. Morphology Control

Yb-, Er-doped CeO_2 hollow nanotubes were synthesized [60] using silver nanowires coated with silica, and the products had a narrower band gap of 2.8 eV. The core–shell structured CeO_2 was converted into mesoporous hollow spheres by the Ostwald ripening method in the presence of urea and hydrogen peroxide [61]. CeO_2 nanocages can be fabricated by mixing $(NH_4)_2Ce(NO_3)_2$ with templates of Cu_2O nanocubes [62], in which Cu_2O is finally sacrificed. The photocatalytic results [63] indicated that CeO_2 nanocages exhibit higher activity than hollow spheres.

Preferentially Exposed Facets

It was found that molecular CO_2 can be distorted and participate in reactions at a low energy on the CeO_2 surface [64]. A p-type NiO material was designed to modify the rod-like CeO_2 nanostructure [65], allowing electrons and holes to migrate to opposite directions. They then operated the Mott–Schottky test, which showed a typical p–n junction. The presence of hexagon-shaped NiO plates broadened the range of light responses, which can be verified in the UV-Vis absorption spectra. Graphene oxide (rGO) was introduced as a “network” of for photoreduction electron transportation (**Figure 12**A–C). The impedance can be seen in the EIS Nyquist plot, which shows that the NiO/CeO_2/rGO achieved the minimum value. The HCHO production rate of the ultimate catalyst was 421 μmol $g^{-1}h^{-1}$ with the synergy of several favorable factors. It is worth mentioning that a range of in situ techniques have been used to detect oxygen vacancies, structural changes, free radicals and formate on the surface of CeO_2.

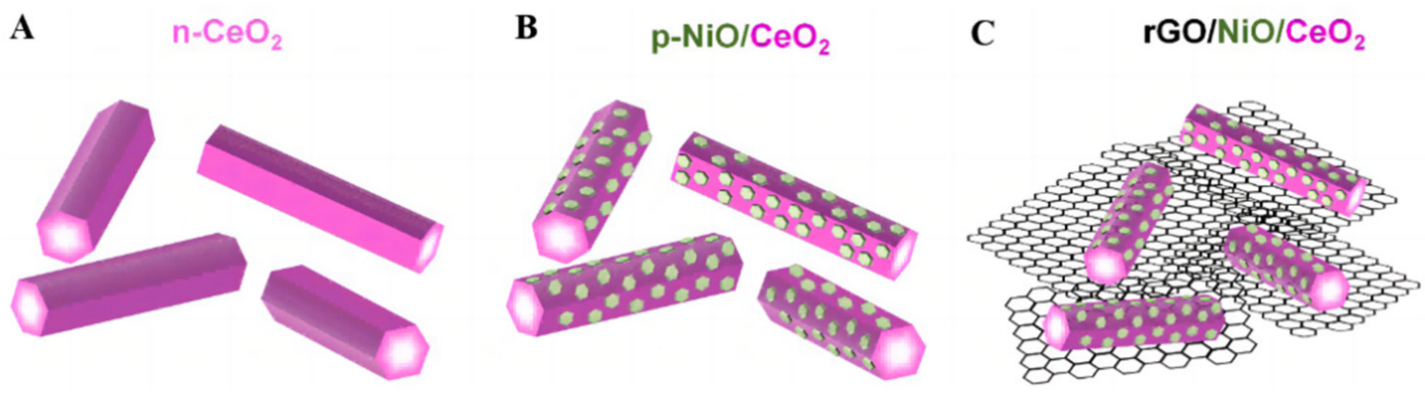

Figure 12. The structural diagrams of (**A**) n-CeO_2 nanorods, (**B**) p-NiO/CeO_2 composite and (**C**) NiO/CeO_2/rGO hybrid composite [65].

Macroporous

Mesoporous N-doped CeO_2(NMCe), a relatively ordered intermediate structure with enhanced CO_2-capturing capability, was prepared without any convoluted procedures or expensive equipment [58]. In the Roman spectrum, the bands from 550 to 650 cm^{-1}, which are closely related to oxygen vacancy, were more salient than the MCe band. In addition, N-doped porous CeO_2 has a higher CO_2 absorption capacity than porous CeO_2.

3DOM Structure Ce-Based Materials

Under the protection of poly alcohol, Zhang et al. [66] synthesized 3DOM CeO_2 that was loaded with Au–Pd alloys. 3DOM CeO_2 photocatalytic materials are expected to emerge in the field of CO_2 emission reduction, which could open up more possibilities for the development of super-catalysts.

3.5.2. Heterojunction

Researchers tried to combine CeO_2 with g-C_3N_4, which is popular for its energy bands and chemical stability. Through hard work, a three-dimensional porous g-C_3N_4(3DCN) was achieved, with the advantages of multi-channel structure. To accommodate more electrons and heighten the density of photoelectric currents, Zhao et al. [59] loaded Pt nanoparticles (5–6 nm) on CeO_2/3DCN using photodeposition techniques that require UV lamp radiation. The photoreduction rate gradually increased as the CeO_2 amount rose in the range of 15~45% and the yield rates of 4.69 and 3.03 $\mu mol \cdot h^{-1} \cdot g^{-1}$ for CO and CH_4 were achieved, respectively, after decorating with Pt crystalline grains.

4. Other 3DOM Materials

In order to introduce advanced porous structures to slow the self-aggregation of quantum dots, Wang et al. [67] devised 3DOM N-doped carbon (NC) to support CdS and ZnO QDs (**Figure 13**). They filled the interspace in an ordered PS microsphere template and then employed a pyrolytic treatment and in situ growth methods. Compared to bulky CdS, the 3DOM compounds have a larger cathodic current density and enhanced light harvesting, bearing a satisfactory carbon monoxide yield of 5210 $\mu mol\ g^{-1}\ h^{-1}$. A three-dimensional SnO_2 inverse opal structure was synthesized as gas sensors, soot oxidation catalyst and photoanode. The 3DOM $BiVO_4$/SnO_2 heterostructure was obtained by adding a $BiVO_4$ precursor to fill the space between SnO_2 skeleton and periodic PS template. The compatibility of energy states with SnO_2 significantly reduced their photoluminescence intensity. Meanwhile, Au nanoparticles enhanced the slow photon effect, which in turn increased the incident light utilization efficiency.

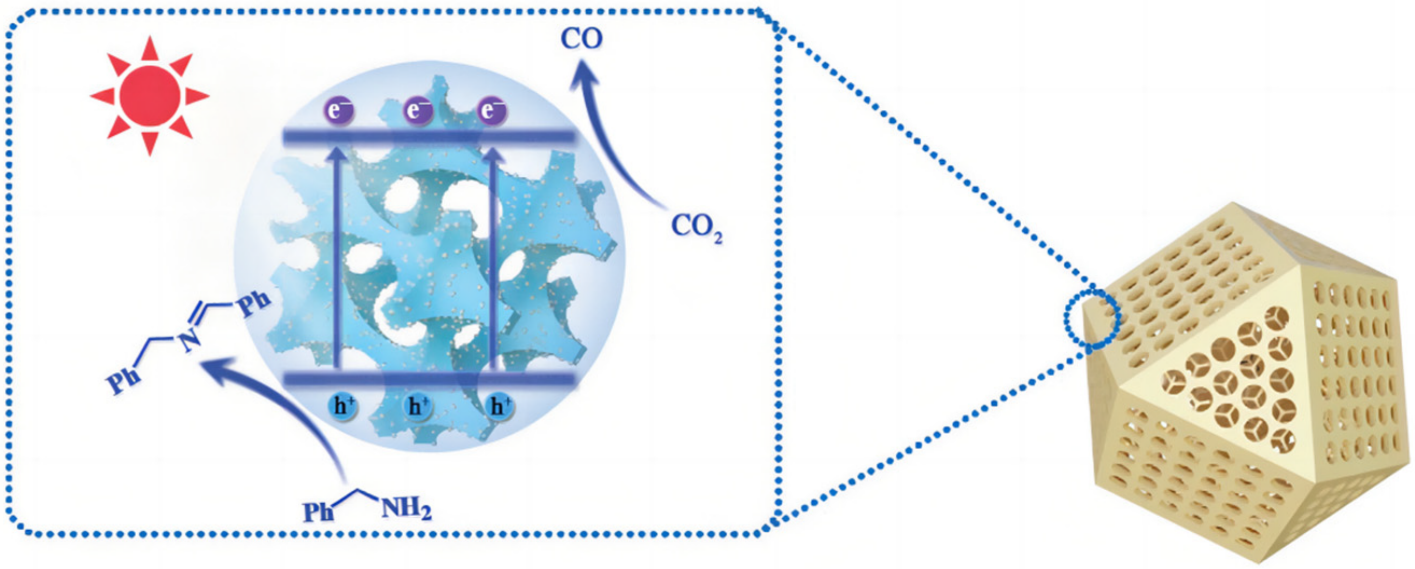

Figure 13. Proposed mechanism for the photocatalytic CO_2 reduction on 3DOM CdS QD/NC. Schematic illustration of the photocatalytic CO_2 reduction coupled with selective arylamine oxidation reaction system [67].

References

1. Fu, S.; Zhang, B.; Hu, H.; Zhang, Y.; Bi, Y. ZnO nanowire arrays decorated with PtO nanowires for efficient solar water splitting. Catal. Sci. Technol. 2018, 8, 2789–2793.
2. Xu, Y.; Han, J.; Luo, Y.; Liu, Y.; Ding, J.; Zhou, Z.; Liu, C.; Zou, M.; Lan, J.; Nan, C.-w.; et al. Enhanced CO2 Reduction Performance of BiCuSeO-Based Hybrid Catalysts by Synergetic Photo-Thermoelectric Effect. Adv. Funct. Mater. 2021, 31, 2105001.
3. Tang, R.F.; Wang, H.; Dong, X.A.; Zhang, S.H.; Zhang, L.L.; Dong, F. A ball milling method for highly dispersed Ni atoms on g-C3N4 to boost CO2 photoreduction. J. Colloid Interface Sci. 2023, 630, 290–300.
4. Shen, H.; Peppel, T.; Stunk, J.; Sun, Z. Photocatalytic Reduction of CO2 by Metal-Free-Based Materials: Recent Advances and Future Perspective. Solar Rrl 2020, 4, 1900546.
5. Irfan, S.; Khan, S.B.; Lam, S.S.; Ong, H.C.; Din, M.A.U.; Dong, F.; Chen, D.L. Removal of persistent acetophenone from industrial waste-water via bismuth ferrite nanostructures. Chemosphere 2022, 302, 134750.
6. Liu, L.; Wang, S.; Huang, H.; Zhang, Y.; Ma, T. Surface sites engineering on semiconductors to boost photocatalytic CO2 reduction. Nano Energy 2020, 75, 126799.
7. Zhang, D.Q.; Mao, B.D.; Li, D.; Liu, Y.H.; Li, F.H.; Dong, W.X.; Jiang, T.Y.; Shi, W.D. 0D/2D Z-scheme heterojunctions of Zn-AgIn5S8 QDs/alpha-Fe2O3 nanosheets for efficient visible-light-driven hydrogen production. Chem. Eng. J. 2021, 417, 128275.

8. Nasir, M.S.; Yang, G.R.; Ayub, I.; Wang, S.L.; Yan, W. In situ decoration of g-C3N4 quantum dots on 1D branched TiO2 loaded with plasmonic Au nanoparticles and improved the photocatalytic hydrogen evolution activity. Appl. Surf. Sci. 2020, 519, 146208.
9. Li, M.; Ma, L.N.; Luo, L.; Liu, Y.G.; Xu, M.; Zhou, H.; Wang, Y.; Li, Z.H.; Kong, X.G.; Duan, H.H. Efficient photocatalytic epoxidation of styrene over a quantum-sized SnO(2)on carbon nitride as a heterostructured catalyst. Appl. Catal. B. 2022, 309, 121268.
10. Xiong, H.; Dong, Y.; Liu, D.; Long, R.; Kong, T.; Xiong, Y. Recent Advances in Porous Materials for Photocatalytic CO2 Reduction. J. Phys. Chem. Lett. 2022, 13, 1272–1282.
11. Liu, J.; Zhao, H.; Wu, M.; Van der Schueren, B.; Li, Y.; Deparis, O.; Ye, J.; Ozin, G.A.; Hasan, T.; Su, B.L. Slow Photons for Photocatalysis and Photovoltaics. Adv. Mater. 2017, 29, 1605349.
12. Zhao, H.; Hu, Z.; Liu, J.; Li, Y.; Wu, M.; Van Tendeloo, G.; Su, B.-L. Blue-edge slow photons promoting visible-light hydrogen production on gradient ternary 3DOM TiO2-Au-CdS photonic crystals. Nano Energy 2018, 47, 266–274.
13. Li, J.F.; Zhong, C.Y.; Huang, J.R.; Chen, Y.; Wang, Z.; Liu, Z.Q. Carbon dots decorated three-dimensionally ordered macroporous bismuth-doped titanium dioxide with efficient charge separation for high performance photocatalysis. J. Colloid Interface Sci. 2019, 553, 758–767.
14. Wang, P.F.; Zhan, S.H. Shedding light on the role of interfacial chemical bond in heterojunction photocatalysis. Nano Res. 2022, 15, 10158–10170.
15. Li, X.; Yu, J.; Jaroniec, M. Hierarchical photocatalysts. Chem. Soc. Rev. 2016, 45, 2603–2636.
16. Yan, X.W.; Wang, B.; Zhao, J.Z.; Liu, G.P.; Ji, M.X.; Zhang, X.L.; Chu, P.K.; Li, H.M.; Xia, J.X. Hierarchical columnar ZnIn2S4/BiVO4 Z-scheme heterojunctions with carrier highway boost photocatalytic mineralization of antibiotics. Chem. Eng. J. 2023, 452, 139271.
17. Ji, M.X.; Feng, J.; Zhao, J.Z.; Zhang, Y.; Wang, B.; Di, J.; Xu, X.Y.; Chen, Z.R.; Xia, J.X.; Li, H.M. Defect-Engineered Bi24O31Cl10 Nanosheets for Photocatalytic CO2 Reduction to CO br. ACS Appl. Nano Mater. 2022, 5, 17226–17233.
18. Bai, S.; Zhang, N.; Gao, C.; Xiong, Y.J. Defect engineering in photocatalytic materials. Nano Energy 2018, 53, 296–336.
19. Shown, I.; Samireddi, S.; Chang, Y.C.; Putikam, R.; Chang, P.H.; Sabbah, A.; Fu, F.Y.; Chen, W.F.; Wu, C.I.; Yu, T.Y.; et al. Carbon-doped SnS2 nanostructure as a high-efficiency solar fuel catalyst under visible light. Nat. Commun. 2018, 9, 169.
20. Wan, S.P.; Ou, M.; Wang, X.M.; Wang, Y.A.; Zeng, Y.Q.; Ding, J.; Zhang, S.L.; Zhong, Q. Facile fabrication of oxygen and carbon co-doped carbon nitride nanosheets for efficient visible light photocatalytic H2 evolution and CO2 reduction. Dalton Trans. 2019, 48, 12070–12079.

21. Zhang, D.P.; Li, Y.X.; Li, Y.; Zhan, S.H. Towards single-atom photocatalysts for future carbon-neutral application. Smartmat 2022, 3, 417–446.
22. Kim, A.; Debecker, D.P.; Devred, F.; Dubois, V.; Sanchez, C.; Sassoye, C. CO2 methanation on Ru/TiO2 catalysts: On the effect of mixing anatase and rutile TiO2 supports. Appl. Catal. B. 2018, 220, 615–625.
23. Yang, X.; Tan, F.; Wang, D.; Feng, Q.; Qiu, D.; Dang, D.; Wang, X. Entrapping Ru nanoparticles into TiO2 nanotube: Insight into the confinement synergy on boosting pho-thermal CO2 methanation activity. Ceram. Int. 2021, 47, 27316–27323.
24. Kar, P.; Farsinezhad, S.; Mahdi, N.; Zhang, Y.; Obuekwe, U.; Sharma, H.; Shen, J.; Semagina, N.; Shankar, K. Enhanced CH4 yield by photocatalytic CO2 reduction using TiO2 nanotube arrays grafted with Au, Ru, and ZnPd nanoparticles. Nano Res. 2016, 9, 3478–3493.
25. Hu, X.L.; Song, J.Y.; Luo, J.L.; Zhang, H.; Sun, Z.M.; Li, C.Q.; Zheng, S.L.; Liu, Q.X. Single-atomic Pt sites anchored on defective TiO2 nanosheets as a superior photocatalyst for hydrogen evolution. J. Energy Chem. 2021, 62, 1–10.
26. Zalfani, M.; Hu, Z.Y.; Yu, W.B.; Mahdouani, M.; Bourguiga, R.; Wu, M.; Li, Y.; Van Tendeloo, G.; Djaoued, Y.; Su, B.L. BiVO4/3DOM TiO2 nanocomposites: Effect of BiVO4 as highly efficient visible light sensitizer for highly improved visible light photocatalytic activity in the degradation of dye pollutants. Appl. Catal. B. 2017, 205, 121–132.
27. Tahir, M.S.; Manzoor, N.; Sagir, M.; Tahir, M.B.; Nawaz, T. Fabrication of ZnFe2O4 modified TiO2 hybrid composites for photocatalytic reduction of CO2 into methanol. Fuel 2021, 285, 119206.
28. Qiu, B.C.; Xing, M.Y.; Zhang, J.L. Recent advances in three-dimensional graphene based materials for catalysis applications. Chem. Soc. Rev. 2018, 47, 2165–2216.
29. Zhang, H.; Wang, X.Y.; Li, N.; Xia, J.H.; Meng, Q.M.; Ding, J.C.; Lu, J. Synthesis and characterization of TiO2/graphene oxide nanocomposites for photoreduction of heavy metal ions in reverse osmosis concentrate. RSC Adv. 2018, 8, 34241–34251.
30. Mgolombane, M.; Bankole, O.M.; Ferg, E.E.; Ogunlaja, A.S. Construction of Co-doped TiO2/rGO nanocomposites for high-performance photoreduction of CO2 with H2O: Comparison of theoretical binding energies and exploration of surface chemistry. Mater. Chem. Phys. 2021, 268, 124733.
31. Lee, J.H.; Kim, S.-I.; Park, S.-M.; Kang, M. A p-n heterojunction NiS-sensitized TiO2 photocatalytic system for efficient photoreduction of carbon dioxide to methane. Ceram. Int. 2017, 43, 1768–1774.
32. Cheng, H.F.; Huang, B.B.; Liu, Y.Y.; Wang, Z.Y.; Qin, X.Y.; Zhang, X.Y.; Dai, Y. An anion exchange approach to Bi2WO6 hollow microspheres with efficient visible light photocatalytic reduction of CO2 to methanol. Chem. Commun. 2012, 48, 9729–9731.

33. Li, B.; Sun, L.; Bian, J.; Sun, N.; Sun, J.; Chen, L.; Li, Z.; Jing, L. Controlled synthesis of novel Z-scheme iron phthalocyanine/porous WO3 nanocomposites as efficient photocatalysts for CO2 reduction. Appl. Catal. B. 2020, 270, 1188849.
34. Wang, L.; Wang, Y.; Cheng, Y.; Liu, Z.; Guo, Q.; Minh Ngoc, H.; Zhao, Z. Hydrogen-treated mesoporous WO3 as a reducing agent of CO2 to fuels (CH4 and CH3OH) with enhanced photothermal catalytic performance. J. Mater. Chem. A 2016, 4, 5314–5322.
35. Rong, R.C.; Wang, L.M. Synthesis of hierarchical hollow nest-like WO3 micro/nanostructures with enhanced visible light-driven photocatalytic activity. J. Alloys Compd. 2021, 850, 156742.
36. Hao, Z.C.; Liu, Z.F.; Li, Y.T.; Ruan, M.N.; Guo, Z.G. Enhanced photoelectrochemical performance of 2D core-shell WO3/CuWO4 uniform heterojunction via in situ synthesis and modification of Co-Pi co-catalyst. Int. J. Hydrog. Energy 2020, 45, 16550–16559.
37. Ling, P.Q.; Zhu, J.C.; Wang, Z.Q.; Hu, J.; Zhu, J.F.; Yan, W.S.; Sun, Y.F.; Xie, Y. Ultrathin Ti-doped WO3 nanosheets realizing selective photoreduction of CO2 to CH3OH. Nanoscale 2022, 14, 14023–14028.
38. Zhang, H.Y.; Tian, W.J.; Li, Y.G.; Sun, H.Q.; Tade, M.O.; Wang, S.B. Heterostructured WO3@CoWO4 bilayer nanosheets for enhanced visible-light photo, electro and photoelectro-chemical oxidation of water. J. Mater. Chem. A 2018, 6, 6265–6272.
39. Hu, Y.F.; Ping, X.C.; Zhang, Y.; Hao, L.; Liu, T.Y.; Zhao, Q.; Lu, Y.; Liu, J.Z. A nanotree-like WO3 film with adjustable defect concentration and its photocatalytic activity. Mater. Sci. Semicond. Process. 2021, 127, 105737.
40. Liang, L.; Li, X.D.; Sun, Y.F.; Tan, Y.L.; Jiao, X.C.; Ju, H.X.; Qi, Z.M.; Zhu, J.F.; Xie, Y. Infrared Light-Driven CO2 Overall Splitting at Room Temperature. Joule 2018, 2, 1004–1016.
41. Chang, Y.; Yu, K.; Zhang, C.; Li, R.; Zhao, P.; Lou, L.-L.; Liu, S. Three-dimensionally ordered macroporous WO3 supported Ag3PO4 with enhanced photocatalytic activity and durability. Appl. Catal. B. 2015, 176–177, 363–373.
42. Tang, Z.; Wang, C.; He, W.; Wei, Y.; Zhao, Z.; Liu, J. The Z-scheme g-C3N4/3DOM-WO3 photocatalysts with enhanced activity for CO2 photoreduction into CO. Chin. Chem. Lett. 2022, 33, 939–942.
43. Xie, Z.; Xu, Y.; Li, D.; Chen, L.; Meng, S.; Jiang, D.; Chen, M. Construction of CuO quantum Dots/WO3 nanosheets 0D/2D Z-scheme heterojunction with enhanced photocatalytic CO2 reduction activity under visible-light. J. Alloys Compd. 2021, 858, 157668.
44. Mohamed, R.M.; Mkhalid, I.A.; Alhaddad, M.; Basaleh, A.; Alzahrani, K.A.; Ismail, A.A. Enhanced CO2 photocatalytic conversion into CH3OH over visible-light-driven Pt nanoparticle-decorated mesoporous ZnO–ZnS S-scheme heterostructures. Ceram. Int. 2021, 47, 26779–26788.

45. Cai, C.; Xu, Y.F.; Chen, H.Y.; Wang, X.D.; Kuang, D.B. Porous nanosheet array for photoelectrochemical reduction of CO2. Electrochim. Acta 2018, 274, 298–305.
46. Xia, W.W.; Mei, C.; Zeng, X.H.; Chang, S.; Wu, G.Q.; Shen, X.S. Mesoporous multi-shelled ZnO microspheres for the scattering layer of dye sensitized solar cell with a high efficiency. Appl. Phys. Lett. 2016, 108, 113902.
47. Tahir, B.; Tahir, M.; Nawawi, M.G.M. Highly sTable 3D/2D WO3/g-C3N4 Z-scheme heterojunction for stimulating photocatalytic CO2 reduction by H2O/H2 to CO and CH4 under visible light. J. CO2 Util. 2020, 41, 101270.
48. Dong, Z.; Wu, Y.; Thirugnanam, N.; Li, G. Double Z-scheme ZnO/ZnS/g-C3N4 ternary structure for efficient photocatalytic H2 production. Appl. Surf. Sci. 2018, 430, 293–300.
49. Wang, Y.; Fan, G.; Wang, S.; Li, Y.; Guo, Y.; Luan, D.; Gu, X.; Lou, X.W. Implanting CoOx Clusters on Ordered Macroporous ZnO Nanoreactors for Efficient CO2 Photoreduction. Adv. Mater. 2022, 34, 2204865.
50. Zhang, P.P.; Zhou, Z.J.; Kou, D.X.; Wu, S.X. Perovskite Thin Film Solar Cells Based on Inorganic Hole Conducting Materials. Int. J. Photoenergy 2017, 2017, 6109092.
51. Li, X.; Wang, Z.; Zhang, J.; Dai, K.; Fan, K.; Dawson, G. Branch-like CdxZn1-xSe/ step-scheme heterojunction for CO2 photoreduction. Mater. Today Phys. 2022, 26, 100729.
52. Yao, S.; Sun, B.Q.; Zhang, P.; Tian, Z.Y.; Yin, H.Q.; Zhang, Z.M. Anchoring ultrafine Cu2O nanocluster on PCN for CO2 photoreduction in water vapor with much improved stability. Appl. Catal. B. 2022, 317, 121702.
53. Zhang, D.F.; Zhang, H.; Guo, L.; Zheng, K.; Han, X.D.; Zhang, Z. Delicate control of crystallographic facet-oriented Cu2O nanocrystals and the correlated adsorption ability. J. Mater. Chem. 2009, 19, 5220–5225.
54. Dong, Y.; Wang, Y.; Cai, T.; Kou, L.; Yang, G.; Yan, Z. Preparation and nitrogen-doping of three-dimensionally ordered macroporous TiO2 with enhanced photocatalytic activity. Ceram. Int. 2014, 40, 11213–11219.
55. Zheng, X.Z.; Han, J.; Fu, Y.; Deng, Y.; Liu, Y.Y.; Yang, Y.; Wang, T.; Zhang, L.W. Highly efficient CO2 reduction on ordered porous Cu electrode derived from Cu2O inverse opals. Nano Energy 2018, 48, 93–100.
56. Liu, S.H.; Lu, J.S.; Pu, Y.C.; Fan, H.C. Enhanced photoreduction of CO2 into methanol by facet-dependent Cu2O/reduce graphene oxide. J. CO2 Util. 2019, 33, 171–178.
57. Flores, F.M.; Luevano, H.E.; Torres, M.L.M.; Do, T.O. CO2 adsorption and photocatalytic reduction over Mg(OH)(2)/CuO/Cu2O under UV-Visible light to solar fuels. Mater. Chem. Phys. 2019, 227, 90–97.

58. Shen, Z.; Xia, Q.; Li, Y.; Yin, C.; Ge, Z.; Li, X.; Wang, Y. Adsorption-enhanced nitrogen-doped mesoporous CeO2 as an efficient visible-light-driven catalyst for CO2 photoreduction. J. CO2 Util. 2020, 39, 101176.
59. Zhao, X.; Guan, J.; Li, J.; Li, X.; Wang, H.; Huo, P.; Yan, Y. CeO2/3D g-C3N4 heterojunction deposited with Pt cocatalyst for enhanced photocatalytic CO2 reduction. Appl. Surf. Sci. 2021, 537, 147891.
60. Zhao, R.F.; Huan, L.; Gu, P.; Guo, R.; Chen, M.; Diao, G.W. Yb,Er-doped CeO2 nanotubes as an assistant layer for photoconversion-enhanced dye-sensitized solar cells. J. Power Sources 2016, 331, 527–534.
61. Yang, Z.J.; Wei, J.J.; Yang, H.; Liu, L.X.; Liang, H.; Yang, Y.Z. Mesoporous CeO2 Hollow Spheres Prepared by Ostwald Ripening and Their Environmental Applications. Eur. J. Inorg. Chem. 2010, 2010, 3354–3359.
62. Ramani, S.; Sarkar, S.; Vemuri, V.; Peter, S.C. Chemically designed CeO2 nanoboxes boost the catalytic activity of Pt nanoparticles toward electro-oxidation of formic acid. J. Mater. Chem. A 2017, 5, 11572–11576.
63. Fang, S.; Xin, Y.; Ge, L.; Han, C.; Qiu, P.; Wu, L. Facile synthesis of CeO2 hollow structures with controllable morphology by template-engaged etching of Cu2O and their visible light photocatalytic performance. Appl. Catal. B. 2015, 179, 458–467.
64. Kumari, N.; Haider, M.A.; Agarwal, M.; Sinha, N.; Basu, S. Role of Reduced CeO2(110) Surface for CO2 Reduction to CO and Methanol. J. Phys. Chem. C 2016, 120, 16626–16635.
65. Park, H.R.; Pawar, A.U.; Pal, U.; Zhang, T.; Kang, Y.S. Enhanced solar photoreduction of CO2 to liquid fuel over rGO grafted NiO-CeO2 heterostructure nanocomposite. Nano Energy 2021, 79, 105483.
66. Zhang, X.; Liu, Y.X.; Deng, J.G.; Yu, X.H.; Han, Z.; Zhang, K.F.; Dai, H.X. Alloying of gold with palladium: An effective strategy to improve catalytic stability and chlorine-tolerance of the 3DOM CeO2 -supported catalysts in trichloroethylene combustion. Appl. Catal. B. 2019, 257, 117879.
67. Wang, F.; Hou, T.; Zhao, X.; Yao, W.; Fang, R.; Shen, K.; Li, Y. Ordered Macroporous Carbonous Frameworks Implanted with CdS Quantum Dots for Efficient Photocatalytic CO2 Reduction. Adv. Mater. 2021, 33, e2102690.